Journal of MATERIALS RESEARCH

Invited Feature Paper
DOI:10.1557/s43578-026-01807-8

MRS DISTINGUISHED INVITED SPEAKER

Structuring, stochastic behavior, and charge storage capacity of redox-active microemulsions formulated with mixtures of toluene and ionic liquid as oil phase

Armando Santiago-Carboney[1], Mrinalini K. Ayilliath Kolaprath[2], Adam Imel[3,4], Mark D. Dadmun[2], Joaquín Rodríguez-López[1,5,a)]

[1] Department of Chemistry, University of Illinois Urbana-Champaign, Urbana, IL 61801, USA
[2] Department of Chemistry, University of Tennessee, Knoxville, TN, USA
[3] Department of Chemical and Biomolecular Engineering, University of Tennessee, Knoxville, TN, USA
[4] University of Tennessee-Oak Ridge Innovation Institute, Oak Ridge, TN, USA
[5] The Beckman Institute for Advanced Science and Technology, University of Illinois Urbana-Champaign, Urbana, IL 61801, USA
[a)] Address all correspondence to this author. e-mail: joaquinr@illinois.edu

Received: 13 November 2025; accepted: 10 February 2026

Oil/water microemulsions (μEs) are promising electrolytes for redox flow batteries (RFBs) as they simultaneously improve charge capacity and ionic conductivity. Here, we report the successful formulation of bicontinuous μEs where the oil phase is a solution of trihexyltetradecylphosphonium bis(trifluoromethylsulfonyl)amide ionic liquid in toluene with redox-active ferrocene. We examined the effect of supporting electrolyte anion (NO_3^-, Cl^-, ClO_4^-) on the structure, reactivity, transport, and electrolytic performance of redox-active μEs. Neutron scattering and nuclear magnetic resonance showed that the domain size increased as $Cl^- > NO_3^- > ClO_4^-$ while the ferrocene diffusion coefficient increased as $NO_3^- > Cl^- > ClO_4^-$. Scanning electrochemical microscopy indicated anion-dependent current fluctuations during electrolysis, with ClO_4^- exhibiting the least high-frequency oscillations, which correlate to the highest charge and discharge capacity and reversibility. All ionic liquid containing systems improved the performance of toluene-based μEs, highlighting new design principles for these electrolytes.

Introduction

Large-scale energy storage devices are promising solutions to the challenges posed by the intermittent nature of renewable energy sources such as solar and wind [1–3]. Redox flow batteries (RFBs) in particular exhibit a low environmental impact, long storage life, and easy scalability technology, making them suitable candidates for storing these inputs [1, 4]. Unlike conventional batteries, RFBs decouple power and energy density. Redox-active components typically take the form of a liquid-electrolyte solution stored in large external tanks that can later be circulated and flowed through electrodes [5]. Therefore, the concentration and volume of the tanks directly affect the energy storage capacity, while the electrodes and cell performance determine the system's power density [5]. Thus, the electrolyte selection will impact the RFB's performance. Aqueous systems have the advantage of being non-flammable and have high ionic conductivity, but water's limited operational voltage window limits the energy storage density. Non-aqueous systems tend to be stable in a wider potential window, but their flammability and low conductivity are their main drawbacks [5, 6].

The ability to combine both aqueous and non-aqueous phases in a thermodynamically stable fluid has made microemulsions (μEs) a suitable alternative electrolyte for RFBs [7, 8]. These thermodynamically stable systems are characterized by being optically clear nanoscale dispersions of two immiscible liquids mixed with surfactants [7–9]. Their versatility lies in their ability to be tuned to meet specific needs through the addition of additives like salts, cosurfactants, and other molecules of interest, such as redox-active species [10, 11]. Ionic liquids (ILs) have been previously employed in microemulsions [12–16]. Such microemulsions have been employed for a

variety of applications ranging from synthesis [17] and catalysis [18–21], to drug delivery [22] and compound extraction [23]. IL-based microemulsions have used in electrochemistry primarily for electrodeposition and synthesis [20, 21], but except for a few papers, they have not been thoroughly explored for long-term electrochemical storage [24, 25], and not for RFBs. Room temperature ILs are usually defined as salts with melting points below 100 °C; therefore, these ambient temperature liquids are mostly comprised ions [26, 27]. ILs have high thermal and chemical stability, are non-volatile and non-combustible, and most importantly, exhibit better electrochemical stability and a wider operational voltage window than water [28, 29]. However, the molecular charge density in these systems is highly nonuniform due to their inherent structure. Therefore, the short-range ion–ion interactions, molecular shape, and ion molecular charge distribution are important for both the bulk and microscale at interfaces [30].

Previously, we studied redox-active μEs formulated with ferrocene as the redox-active component and toluene as the non-aqueous phase, and reported stochastic behavior when analyzing these electrolytes with scanning electrochemical microscopy (SECM) [8]. Given the complex structure of μEs, we reasoned that SECM, which allows us to constrain the liquid between two electrodes (~ 500 nm gap), could yield a measurable signal to understand their microscale interfacial dynamics during prolonged electrolysis [31]. The SECM is a valuable technique that has been previously employed to study the performance of a variety of battery systems, using an SECM tip (i.e., a nano- or ultramicroelectrode) that reports on the electrochemistry within a tip-substrate gap [8, 32–34]. In the feedback mode of SECM, if the tip is in proximity to an insulating surface (negative feedback), the diffusion of the redox mediator is hindered, and a decrease in the tip current is expected with respect to that of the bulk. In contrast to this mode, in positive feedback the tip is close to a conducting surface, and due to redox cycling between the tip and the surface, the current measured at the SECM tip increases relative to that in the bulk. In the Substrate-Generation/Tip-Collection mode, the conducting surface generates an electroactive species that diffuses to the tip, where it is collected [34].

Because μEs formulated with toluene suffer from low conductivity in the oil phase and do not readily dissolve polar and charged species [8], we decided to explore a new formulation that simultaneously addresses conductivity and polarity while retaining the ability to form a bicontinuous μE. In this work, we present a novel μE system based on a mixture of toluene and trihexyltetradecylphosphonium bis(trifluoromethylsulfonyl) amide ($[P_{66614}][TFSI]$) ionic liquid, a common non-ionic surfactant, polysorbate 20, and water. First, we analyze the structural aspects of these μEs using neutron scattering methods. To deepen the understanding of the system, we analyzed the electrochemical performance of the μEs as a function of the supporting electrolyte dissolved in the aqueous phase, and compared them to the performance of previously formulated μEs as well as those containing different anions, establishing valuable correlations with their bulk electrolysis performance which help us better design electrolytes for RFBs.

Results and discussion

We designed a set of μEs containing 40% water, 55% surfactant, and 5% oil. As observed in Fig. 1(A), both the surfactant and oil phases are composed of two different components. The surfactant is made up of 30% (wt.) 1-butanol dissolved in polysorbate 20, while the oil is composed of 40% (wt.) $[P_{66614}][TFSI]$ in toluene. After formulating a large stock of the μE, it was divided into three containers. In each container, 20 mM ferrocene (Fc) was dissolved, and either KNO_3, KCl, or $KClO_4$ was dissolved at 0.5 M, 0.5 M, and 0.15 M, respectively.

Figure 1(B) shows a picture of the optically clear microemulsion, a key characteristic of the Winsor IV (W4) system [7, 8, 35]. The color comes from the dissolved Fc, and the arbitrary

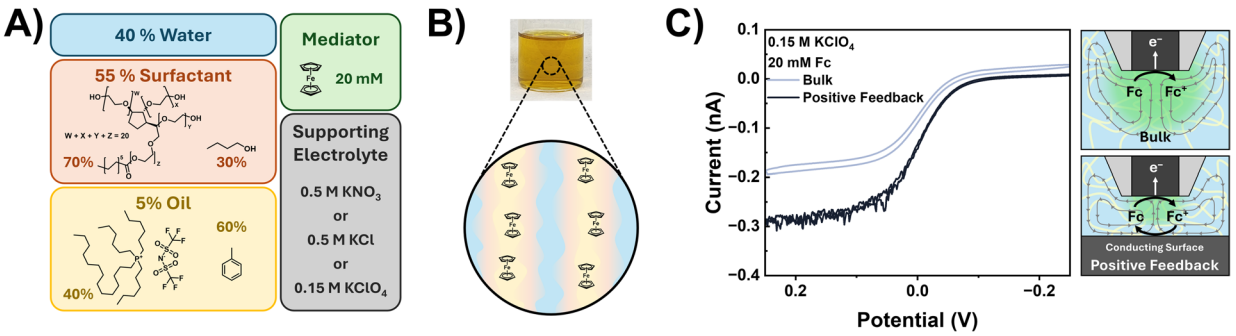

Figure 1: Composition, structure, and preliminary experiments in μEs. (A) Structure and composition of the elements in the μE, highlighting what is present in each phase. (B) Picture of the optically clear μE and an arbitrary schematic of its nanostructure. (C) Cyclic voltammetry during two different SECM modes (schematics) showing the appearance of current fluctuations at the mass transfer-limited region.

schematic of the microemulsion's nanostructure is meant to represent the system's phases with the Fc dissolved in the oil phase. Cyclic voltammetry (CV) experiments in Fig. 1(C) show that the sigmoidal wave changes with the SECM mode employed. A smooth sigmoidal shape is observed when the SECM tip is at the bulk, while the positive feedback mode shows the appearance of current fluctuations due to the convection in the system.

Microemulsion characterization

Figure 2 shows the fish and pseudo-ternary phase diagrams required for the optimization of the μE. To form the fish diagram, we explored the cosurfactant-to-surfactant mass ratio (M_{CS}/M_S) against total microemulsion composition, employing the cosurfactant (M_{CS}) and surfactant (M_S) fraction in a system with equal volume parts of water (V_W) and oil (V_O), two immiscible liquids. This relationship directly impacts the curvature of the surfactant membrane formed at the boundary between the oil and water phases [36, 37]. A visual representation of the curvature is observed in the y-axis of a fish diagram. In Fig. 2(A) the microemulsion region, also known as Winsor IV type (W4), is highlighted in red, and an arbitrary red line was added to aid in the visualization of the "fish tail" obtained. As reported by Arleth et al., the beginning of the fish tail on the right side of the red region corresponds to a bicontinuous microemulsion, while further to the left leads to the formation of lamellae [37]. From the diagram, the composition of the right-most red point was selected to determine the most effective 1-butanol concentration of 30% (w/w) in polysorbate 20. Even though the system comprises four components, mixing 30% (w/w) 1-butanol in polysorbate 20 allows the formation of a pseudo-ternary diagram that delimits the region where a 1-phase system is thermodynamically stable, thus forming a μE. In Fig. 1(B), such a ternary diagram is observed. We decided to maximize the water content, as our previous work showed that it is directly proportional to the system's conductivity [8]. The brown point in Fig. 1(B) corresponds to a μE with the volumetric composition of 40% water, 5% oil, and 55% surfactant. To understand the system, we characterized the structure and electrochemical performance of that exact composition as a function of the supporting electrolyte dissolved in the water phase.

Small-angle neutron scattering (SANS) results indicate that the type and concentration of supporting electrolyte have only a minor influence on the nanostructure of the microemulsion (μE) [Fig. 3(A)]. The scattering data were fit using the Teubner–Strey (T–S) model, which has been shown to provide the most accurate description of bicontinuous μEs [7, 38]. Developed through an expansion of the Landau free energy, the T–S model captures the characteristic scattering peak observed in the one-dimensional profiles of bicontinuous micelles and μEs [39].

From the T–S fits, four key structural parameters were extracted: domain size (d), correlation length (ξ), amphiphilicity factor (f_a), and bending rigidity (κ_{SANS}). The domain size represents the distance half-way in a water domain to half-way in an adjacent water domain, while the correlation length describes the distance over which a structural correlation is maintained [40]. The amphiphilicity factor quantifies the extent of the microemulsion ordering with its value ranges from + 1 (completely disordered) to – 1 (well-ordered lamellar) [41–44].

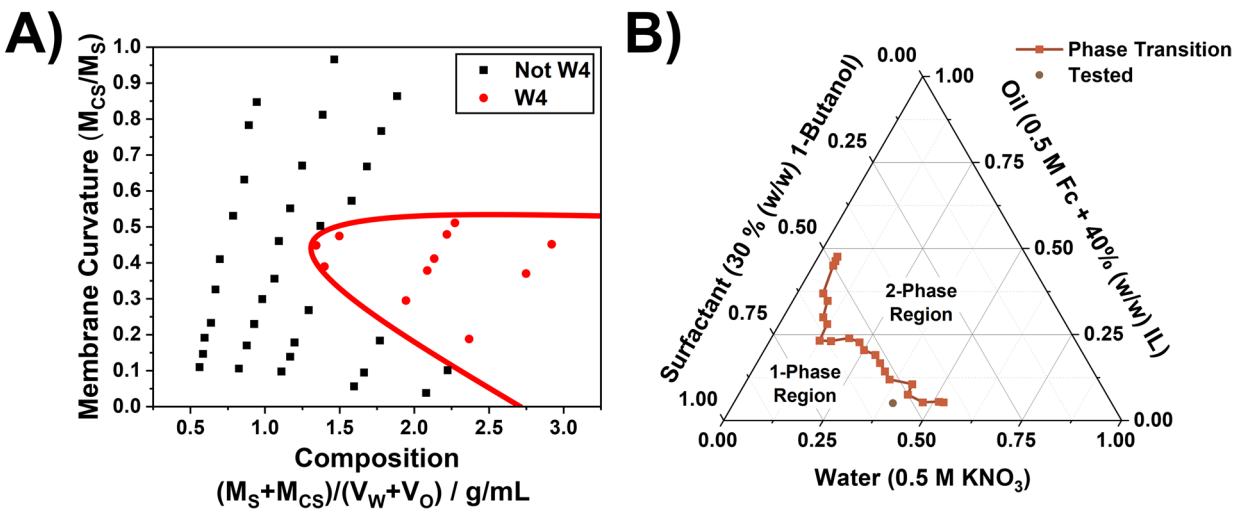

Figure 2: Fish and Phase diagrams for the toluene-[P_{66614}][TFSI] system. (A) Fish diagram showing the region where a Winsor IV (W4) type μE is formed (red), leading to the optimization of the 1-butanol content. The diagram compares the cosurfactant-to-surfactant mass ratio (M_{CS}/M_S) with the mass-to-volume ratio of the cosurfactant and surfactant (M_{CS} and M_S, respectively) to the water and oil volume content (V_W and V_O, respectively). An arbitrary red line was added to improve the visualization of the fish tail. (B) Pseudo-ternary phase diagram resulting after the 1-butanol optimization, showing the 1-phase region indicating the compositions leading to a W4-type μE.

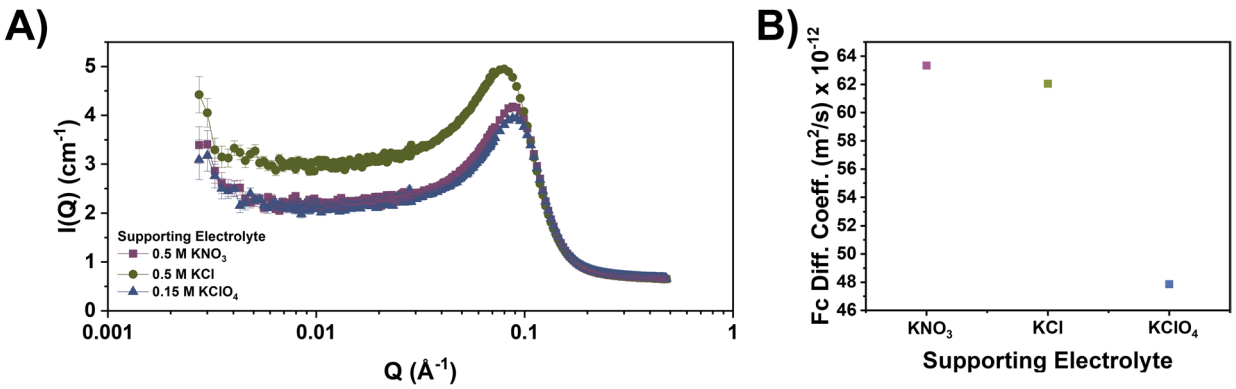

Figure 3: Microemulsion characterization via spectroscopic methods. (A) Shows the small-angle neutron scattering pattern characteristic of a bicontinuous μE for the different supporting electrolytes employed. (B) Self-diffusion coefficient of ferrocene (Fc) in the microemulsions calculated via DOSY-NMR as a function of the supporting electrolyte in solution.

Finally, the bending rigidity (in k_BT units) describes the amount of energy necessary to bend the interface from the equilibrium curvature [45, 46].

As summarized in Table 1, μEs containing $KClO_4$ have the smallest domain size, KNO_3 shows the largest correlation length, and KCl has the largest domain size and smallest correlation length. The decreased correlation length, higher amphiphilicity factor and lower bending rigidity associated with KCl suggest a more disordered and flexible microemulsion. There is literature reporting the domain size, correlation length, amphiphilicity factor, and bending rigidity for μEs made with KNO_3 in the water phase, Fc in toluene for the oil phase, and a 17.5% (wt.) butanol solution in polysorbate 20 as the surfactant [7]. We have included that information in Table 1 for ease of comparison. Our μEs show a decrease in the domain size and correlation length, while only KNO_3 and $KClO_4$ have an amphiphilicity factor that resembles that of the literature, all while being less rigid than previously published results, likely due to the increased amount of butanol used in this study. In the literature, differences in water-anion interactions and their effects on solvation have been noted [47–49], and the microemulsion literature shows that butanol partitions between the water and surfactant phases [50]. We believe that the changes in the microemulsion's nanostructure are due to the anion solvation and how this phenomenon has an effect on the water-surfactant-cosurfactant interactions that lead to the lamellae formation.

Via diffusion-ordered spectroscopy nuclear magnetic resonance (DOSY-NMR), we calculated the self-diffusion coefficient of Fc in each of the μEs. To achieve this, we obtained the ^{1}H NMR spectrum for each composition, assigned the peaks according to the literature, and displayed the information in Fig. S2 and Table S2 [51–53]. Although they were all formulated in the same way, Fc shows a distinct diffusion coefficient for each composition, although KNO_3 and KCl show the highest similarity. We want to point out that as the degree of solvation of the supporting electrolyte anion decreases [47–49], the diffusion coefficient of ferrocene not only decreases, but starts to get more similar to that of the surfactant phase. A previous study has suggested that ferrocene can be "stored" in the surfactant phase, facilitating electron transfer [54]. Figure 3(B) shows that the μE formulated with 0.15 M $KClO_4$ displays a smaller diffusion coefficient than that of the other two compositions. The full 2D spectrum obtained after DOSY analysis for each μE is shown in Figs. S3–S5. The ferrocene diffusion coefficient differences and the nanostructural characteristics of the μEs suggest that the anion solvation is an important parameter to consider when formulating redox-active microemulsions.

SECM feedback mode

Cyclic Voltammetry (CV) is a valuable technique for assessing the electrochemical performance of dissolved Fc by examining the shape and peak splitting of its redox process. Here, a larger

TABLE 1: Correlation length (d), domain size (ξ), amphiphilicity factor (f_a), and bending rigidity (κ_{SANS}) of the μEs formulated resulting from the Teubner-Strey fit, and a comparison between a 40% water μE (40W) without ionic liquid from literature [7].

Supporting Electrolyte	Domain size (d) / Å	Correlation length (ξ) / Å	Amphiphilicity factor (f_a)	Bending rigidity (κ_{SANS}) /k_BT
40W in literature [7]	75.7 ± 0.08	34.2 ± 0.16	−0.779	0.384 ± 0.002
0.5 M KNO_3	65.1 ± 0.1	27.5 ± 0.2	−0.75	0.359 ± 0.003
0.5 M KCl	70.9 ± 0.25	26.1 ± 0.1	−0.68	0.313 ± 0.002
0.15 M $KClO_4$	64.2 ± 0.15	26.9 ± 0.3	−0.75	0.359 ± 0.004

peak splitting could result from either increased ionic resistance or increased charge transfer resistance. Our CV results using a disk macroelectrode (A = 0.07 cm^2) show that $KClO_4$ as the supporting electrolyte yields a more resistive solution with higher peak splitting, whereas KCl yields the least resistive solution [Fig. 4(A)]. This behavior is expected, as the maximum $KClO_4$ concentration achieved was 0.15 M, compared to 0.5 M for both KNO_3 and KCl. Still, these results show an improvement in the electrochemical behavior with respect to previously published systems without ionic liquid [8]. The SECM tip voltammetry, which uses an ultramicroelectrode (UME) and is less sensitive to the low ionic conductivity of the electrolyte, shows the characteristic sigmoidal shape expected for a UME voltammogram. Figure 4(B) shows the case where the SECM tip is at the bulk of the solution, and no physical barriers are in the vicinity of the electrode. This leads to a cyclic voltammetry lacking noise-like current fluctuations. Although all compositions have the same Fc loading, the KCl composition shows the highest current, and $KClO_4$ the lowest. This result is in line with the diffusion coefficient trends obtained via DOSY in Fig. 2 and indicates that even though the Fc diffusion coefficient for $KClO_4$ is closer to that of the surfactant phase, the electron transfer kinetics aren't improved. When comparing this information to the SANS fitting in Table 1, we observe that the change in domain size for KCl may explain why it shows the most reversible behavior.

Positioning the SECM tip in the vicinity of an insulating surface (SECM Negative Feedback Mode, NF) results in a decrease in the measured current. Figure 4(C) shows that the physical presence of a surface near the electrode leads to the expected decrease in current due to diffusive blocking, accompanied by strong current fluctuations in the mass-transfer-limited region, as we have already reported for μEs [8]. When the SECM tip is positioned in proximity of a conducting surface (SECM Positive Feedback Mode, PF), the redox cycling of the mediator between the tip and surface increases the current magnitude. In this work, the tip electrode potential was 0.25 V more positive than

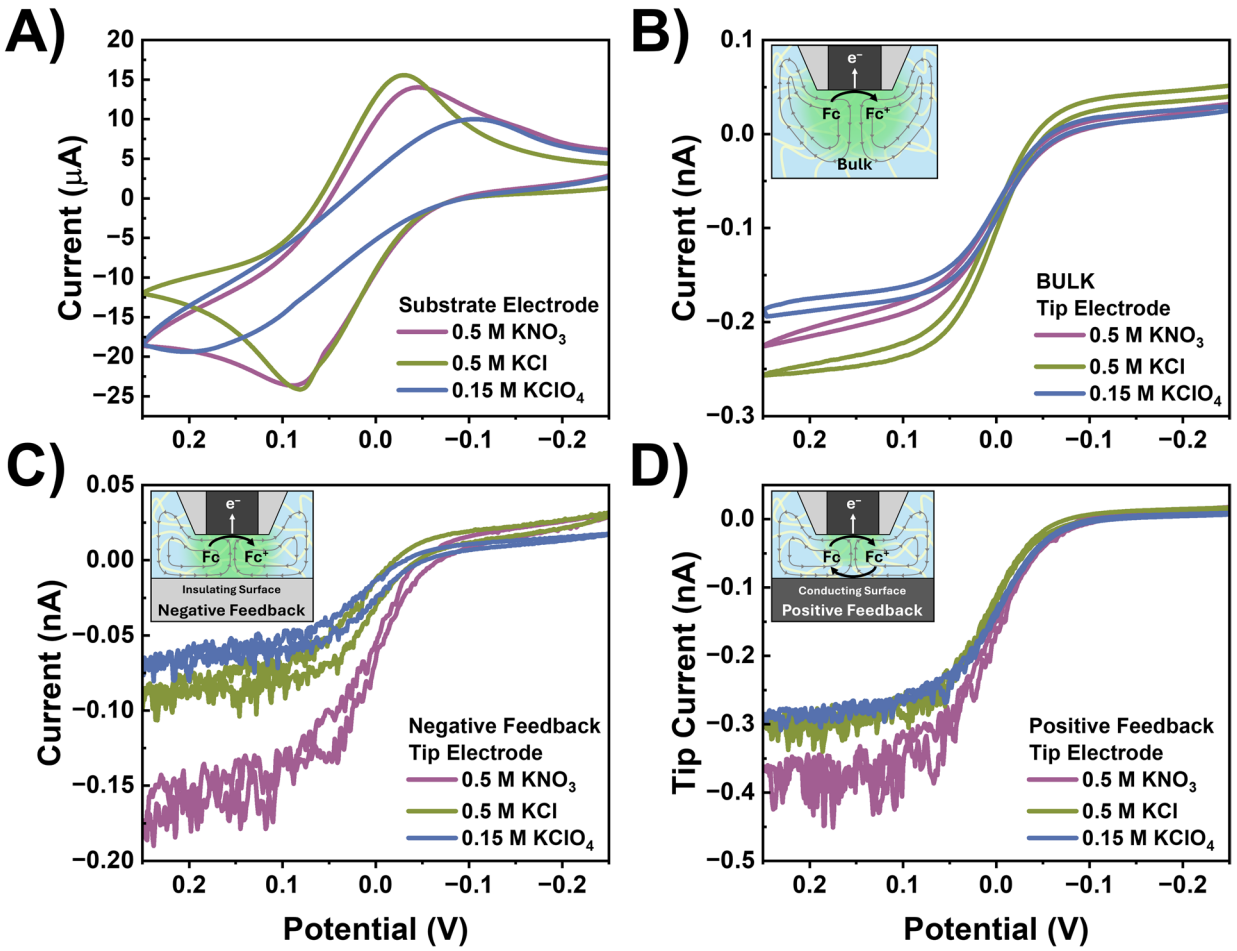

Figure 4: Cyclic voltammetry in microemulsions. (A) Cyclic voltammetry at the disk macroelectrode (A = 0.07 cm^2), showing the characteristic duck-shape of a planar diffusion profile. (B) Cyclic voltammetry at the SECM Tip electrode at the bulk of the solution showing sigmoidal behavior of a semi-hemispherical diffusion profile. (C) Negative feedback (glass surface) and (D) positive feedback (Pt substrate) cyclic voltammograms showing the onset of current fluctuations at the mass-transfer limited region. The inserts in the SECM Tip figures show a cartoon of the SECM mode for reference.

the $E_{1/2}$ of the Fc/Fc^+ redox couple to ensure mass-transfer limited kinetics at the tip, while the Pt conducting substrate potential was set 0.25 V more negative to ensure a sufficiently high rate of redox recycling to generate PF. Figure 4(D) illustrates this effect, as the measured current is larger than that at the bulk and is accompanied by current fluctuations. This highlights that the SECM configuration is key to observing fluctuations in the mass-transfer-limited region, as previously reported [8]. The SECM tip was reproducibly approached to L = 0.35 for both SECM modes, corresponding to a distance of ~ 500 nm, as determined by fitting the approach curves shown in Fig. S1 [55]. The theoretical fit for the negative feedback approach curve predicts a value of $i/i_\infty = 0.332$. The μEs that contained KCl and $KClO_4$ displayed a similar normalized current value, while the μE with KNO_3 showed a normalized current value of $i/i_\infty = 0.73 \pm 0.08$, as seen in Table S1. For the positive feedback, the fit predicts $i/i_\infty = 1.735$, and none of the μEs reached that value. The KNO_3 μE was the closest with just $i/i_\infty = 1.32 \pm 0.10$, and KCl the worst with $i/i_\infty = 1.19 \pm 0.09$, also seen in Table S1.

Surface-Generation/Tip-Collection (SGTC) experiments for the toluene-$[P_{66614}][TFSI]$ μEs in Fig. 5 show that the current fluctuations are also present when the substrate is polarized to electrolyze Fc. However, the contribution of these fluctuations is observed only at the SECM tip, with an almost-sigmoidal response at the tip electrode, consistent with the literature [56]. Previous studies using only toluene as the oil phase showed a significant disparity in the collected current at the SECM tip. We suggested that these differences arise from differences in diffusion coefficient between Fc and Fc^+, due to their partitioning between the water and oil phases, as toluene is not polar enough to dissolve Fc^+ [8]. In the Toluene-$[P_{66614}][TFSI]$ system, the shape of the SECM tip current suggests that such a disparity is not present for the redox pair Fc/Fc^+. The addition of the IL results in an overall improvement in SGTC behavior, suggesting greater stabilization of the Fc^+ ion [8]. Still, we find differences between the normalized current during positive feedback and that one during generation/collection. The calculated values are shown in Table S1. For all μEs, the calculated i/i_∞ was larger than expected for the positive feedback approach curve. This disparity can also be observed when comparing the currents in Figs. 4 and 5, KCl had the smallest normalized current in this mode, with $i/i_\infty = 2.47 \pm 0.06$, while the largest value, $i/i_\infty = 3.30 \pm 0.09$, was measured for $KClO_4$. We suggest that the IL polarity in the oil phase stabilizes the Fc^+ ion, reducing its

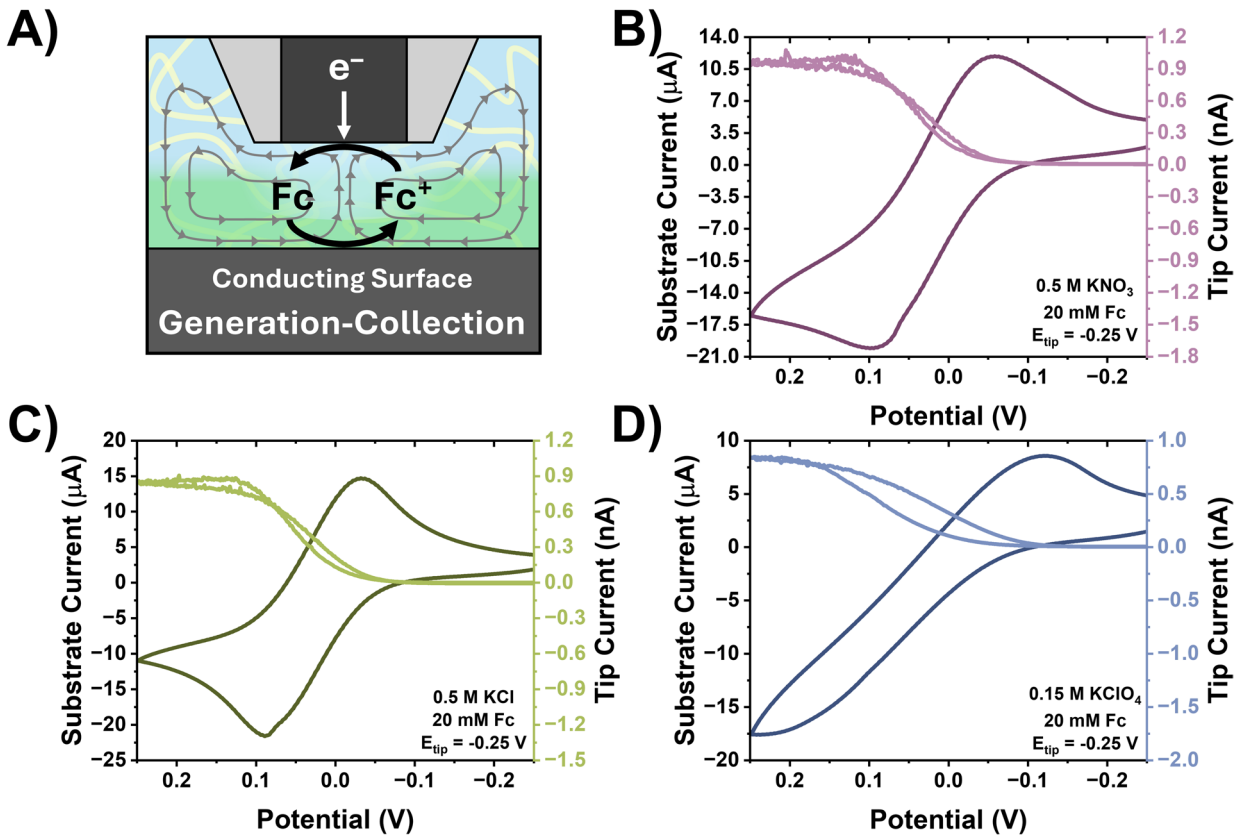

Figure 5: SECM Surface Generation/Tip Collection experiments over a Pt conducting substrate showing the onset of current fluctuations once the mass transfer-limited region is reached. (A) Visual representation of the SECM mode employed when obtaining the generation-collection cyclic voltammetry for (B) 0.5 M KNO_3, (C) 0.5 M KCl, and (D) 0.15 M $KClO_4$.

likelihood of partitioning between the water and oil phases. Given the normalized current results, we think that the complex structure of the μE confines Fc^+ diffusion to the oil phase, thereby aiding redox cycling. Figure 5(D) shows some hysteresis present at the tip electrode, which can correlate to the decreased diffusion coefficient measured in the DOSY-NMR experiment in Fig. 3(B).

Noise analysis

Power spectral density (PSD) analysis of the amperometric response of the mass-transfer limited oxidation of Fc in μEs shows an increase in the noise profile when the μE is constricted to a small volume (Fig. 6). All μEs in Fig. 6 show a linear decrease in the PSD when the SECM tip electrode is far from any obstacle (bulk), and the decay is proportional to $f^{-3/2}$, which is consistent with the literature for systems where mass transfer is limited only by diffusion [57]. A deviation in the PSD decay in both the negative and positive feedback modes suggests that mass transfer is influenced by a process distinct from diffusion. This is easily observed in both feedback modes because the tip placement constricts not only the μE but also the diffusion layer, leading to more noticeable fluctuations from small changes in mass transfer [8]. Previously, we proposed that the Fc/Fc^+ concentration gradient drives Marangoni convection in the diffuse layer around the electrode, leading to current fluctuations. It is well-known that electrode polarization triggers a restructuring of the IL in the vicinity of the electrode surface [30, 58, 59]. The PSD analysis at the bulk for all compositions in Fig. 6 show a slight increase in the contributions at higher frequencies, indicating that even at the bulk, the self-assembly of the IL due to the electrode polarization contributes to the measured current, increasing the mass transfer at the tip electrode, and showing a deviation from the expected decay. In previous studies, we observed that the $f^{-3/2}$ decay in bulk measurements results from the small domain sizes in the microemulsion compared to the tip electrode size [8]. This averages out the individual contributions, but the IL self-assembly is ordered enough to show a change in the PSD. KCl [Fig. 6(C)] shows the most contributions, suggesting that a larger domain size, and lower bending rigidity energy might not improve the electrochemical performance under prolonged electrolysis. The PSD analysis for 0.5 M KNO_3 in Fig. 6(A) shows the largest deviation from the expected behavior for the negative and positive feedback modes, with strong current contributions at a frequency of roughly 2.5 Hz. Given that the 0.5 M KNO_3 μE has the largest domain size, and bending rigidity, this sharp peak at 2.5 Hz might be derived from the self-ordering of the IL. The PSD analysis for 0.5 M KNO_3, and 0.5 M KCl in Fig. 6(A) and (B), respectively, lack the expected decay in the negative and positive feedback modes at lower frequencies, although this is still present for 0.15 M $KClO_4$ in Fig. 6(C). This last one shows a lower deviation from the expected PSD decay compared to the other two compositions. Therefore, the μE formulated with 0.15 M $KClO_4$ results in the composition with the lowest amount of noise-like contributions from the analyzed set, although its overall performance could be skewed by its higher resistivity.

Bulk electrolysis

Repeated oxidation and reduction of the bulk dissolved Fc in the μEs provides information on the system's capacity to store and release energy. Figure 7 shows the normalized charge and discharge curves for each of the μE compositions. All the formulated μEs show higher oxidative currents, as observed in previously published results [8]. Therefore, we consider the current at the end of the reduction cycle as an indicator of the total Fc accessed during oxidation, which we compare to the theoretically available based on the amount of Fc present. Figure 7(A) shows the corresponding composition with 0.5 M KNO_3, with a maximum Fc accessibility of 80% and minimal losses between cycles. The μE with 0.5 M KCl in Fig. 7(B) shows the worst performance, with each cycle showing a roughly 5% loss in Fc access. Figure 7(C) for the μE with 0.15 M $KClO_4$ shows

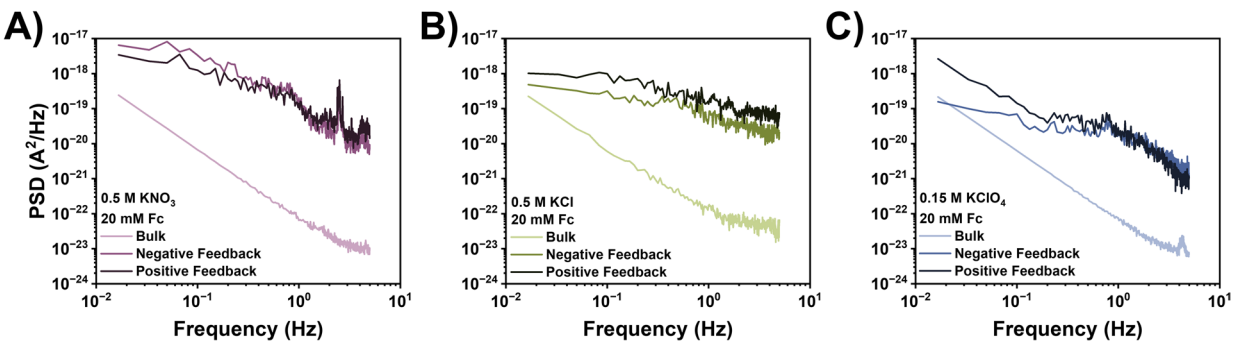

Figure 6: Power Spectral Density analysis of the chronoamperometric curves for (A) 0.5 M KNO_3, (B) 0.5 M KCl, and (C) 0.15 M $KClO_4$ microemulsions. Negative feedback was obtained over a glass surface, and positive feedback was obtained over a Pt conducting substrate.

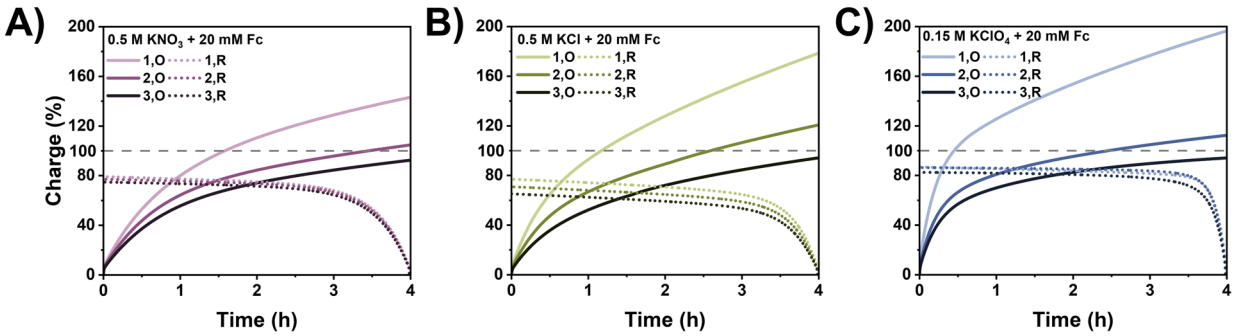

Figure 7: Cyclical bulk electrolysis showing the charge capacity for the (A) 0.5 M KNO_3, (B) 0.5 M KCl, and (C) 0.15 M $KClO_4$ microemulsions. Each plot refers to the Oxidation (O) and Reduction (R) steps, numbered from 1 to 3, corresponding to the cycle.

that we can reproducibly access roughly 85% of the Fc available, with minimal loss between cycles. Although the DOSY-NMR experiments showed a decreased Fc diffusion coefficient for the μE with 0.15 M $KClO_4$, and the CV peak splitting indicated that this composition had the greatest resistance among the analyzed systems, it proved to be the one with the best charge and discharge performance. This could be partly due to the decreased domain size and higher bending rigidity of this composition, as determined by SANS. But also, ion hydration experiments in organic solvents have shown that Cl^- and NO_3^- ions interact more strongly with water molecules than ClO_4^- ions [47–49]. Studies of total water molecules transfer during anion exchange experiments between water and organic solvents showed that NO_3^- ions solvate so strongly that even in low dielectric constant solvents, water molecules transfer in an almost 1:1 (ion: water) ratio, compared to the 1:0.3 or 1:0.4 reported for ClO_4^-, described as a "large poorly solvated anion" [49]. We posit that the decreased solvation of the ClO_4^- ion plays an important role in the charge balance in μEs during charge and discharge, as it can transfer more easily between phases compared to other well-solvated ions like Cl^- and NO_3^-.

After exploring the electrochemical performance of the μE, we observed a correlation between the SANS and DOSY results, as well as convective flow resulting from the electrolysis of Fc in the form of stochastic current fluctuations. The larger domain size observed in the 0.5 M KCl μE led to a better reversibility in the CV experiments, and a large diffusion coefficient, but the PSD indicated an increase in the high-frequency contributions. The 0.15 M $KClO_4$ μE displayed the complete opposite behavior, small domain sizes, a decreased Fc diffusion coefficient, an overall bad electrochemical performance, but its bulk electrolysis, shows the best charge and discharge performance. We posit that such behavior is related to the identity of the anion and its solvation. ClO_4^- shows a decreased solvation compared to the Cl^- and NO_3^-, and therefore its transfer between phases might be facilitated. We highlight that the anion of choice influences the electrolyte's performance, while Cl^- results in better kinetics and a decrease in resistance, ClO_4^- results in the best cyclability and Fc accessibility. While these results suggest a compromise between rate and capacity, all ionic liquid containing systems improved the performance of toluene-based μEs, highlighting new design principles for these electrolytes.

Conclusions

In this work, we describe the electrochemical performance of μEs in relation to the supporting electrolyte anion and the resulting nanostructure obtained via SANS. The oil phase in the μE consisted of a 40% (wt.) $[P_{66614}][TFSI]$ in toluene solution. The redox activity of the μEs stems from the dissolution of 20 mM Fc. Fitting the SANS data to a Teubner-Strey model yielded distinct domain size and correlation length for all μEs, with KNO_3 showing the largest correlation length, $KClO_4$ the smallest domain size, and KCl the largest domain size and smallest correlation length. This last one was also the most disordered and with the least bending rigidity energy. DOSY-NMR experiments show that Fc in the 0.15 M $KClO_4$ μE exhibits a smaller diffusion coefficient, while the other two exhibit a similar value.

Materials and methods

Chemicals

All chemicals were purchased from commercial sources and used as received. The solid chemicals employed were ferrocene (Fc, 98%, Sigma-Aldrich), potassium nitrate (KNO_3, ≥ 99.0%, Sigma-Aldrich), potassium chloride (KCl, ≥ 99.0%, Research Products International), potassium perchlorate ($KClO_4$, 99%, Alfa Aesar), (hydroxymethyl)ferrocene (FcMeOH, ≥ 96.5%, Sigma-Aldrich), potassium phosphate monobasic (KH_2PO_4, ≥ 99.0%, Sigma-Aldrich), and potassium phosphate dibasic (K_2HPO_4, 99.8%, Fisher Chemicals). The liquid chemicals used were 1-butanol (> 99.0%, TCI America), toluene (99.8%, Fisher Scientific), trihexyltetradecylphosphonium bis(trifluoromethylsulfonyl)amide ($[P_{66614}][TFSI]$, ≥ 95.0%, Sigma-Aldrich), Polysorbate 20 (≥ 40%,

Sigma-Aldrich), and nitric acid (HNO_3, > 90%, Sigma-Aldrich). All the aqueous solutions were made using deionized (DI) water from a Milipore Sigma Direct-Q 8 (resistivity of 18.2 MΩ). The UME was fabricated using a 0.002 mm diameter Pt Wollaston wire (99.9%, Goodfellow Cambridge Limited), borosilicate glass capillaries (OD: 1.5 mm, ID: 0.84 mm, World Precision Instruments), 3 inches in length, and silver conductive epoxy (H20E EPO-TEK ®). The SECM surface was achieved using a microscope glass slide (VWR International), and the connection between the conductive side and the potentiostat was achieved with an indium wire (99.998 + %, Thermo Scientific Chemicals) and copper conductive tape (3 M). To clean and degrease, isopropanol (99%, Honeywell) and acetone (99.5%, Fisher Scientific) were used.

Diagram and microemulsion preparation

Fresh stock solutions of 0.5 M KNO_3 and 40% $[P_{66614}][TFSI]$ in toluene were made to serve as the water and oil phases, respectively. Employing an analytical balance (Mettler Toledo XS105 Dual Range), different amounts of 1-butanol and polysorbate 20 were weighed in 4.5 mL glass scintillation vials. Equal amounts of the water and oil phases were pipetted into the scintillation vials containing the polysorbate 20/1-butanol mix. The vials were vigorously shaken and classified as a Winsor IV type microemulsion (W4) if the contents appeared to be a single phase and optically clear to the naked eye, as described in the literature [7, 8, 35]. A fresh stock solution of 30% (wt.) 1-butanol in polysorbate 20 was made to serve as the surfactant phase, along with the previously mentioned water and oil phases. Different ratios of water and oil were pipetted into 4.5 mL scintillation vials. The surfactant phase was placed in a 50 mL burette, and each scintillation vial was titrated dropwise while stirring until a homogeneous, optically clear solution was achieved. The solutions were allowed to stabilize overnight, and to ensure the W4 region was reached, few drops of the surfactant phase were titrated to confirm there were no phase changes. Fresh stock solutions of oil and surfactant were made before preparing the μE, while pure DI water was used for the water phase. A 50 mL stock of μE was created with the following volume fraction: 40% water, 5% oil, and 55% surfactant. Using this stock solution and volumetric flasks, supporting electrolytes and Fc were added to create three compositions: one μE with 0.5 M KNO_3, another with 0.5 M KCl, and finally one with 0.15 M $KClO_4$, all containing 20 mM Fc. Solubility tests were conducted, and the selected concentrations were determined by maximizing both the supporting electrolyte and redox species content.

Instrumentation

Measurements were performed using a CHI 920D Scanning Electrochemical Microscope from CH Instruments Inc. and a Reference 3000 Potentiostat from Gamry Instruments Inc. As a counter electrode, a commercial platinum wire was used, while an Ag/AgCl (3M KCl) reference electrode was placed in the cell via a 0.1 M $NaClO_4$|agar salt bridge. The UME was fabricated using a Narishige PE-2 microelectrode puller from Narishige Group. SECM substrates were cleaned using a PDC-001-HP plasma cleaner from Harrick Plasma. Diffusion-Ordered Spectroscopy Nuclear Magnetic Resonance (DOSY-NMR) measurements were made using a four-channel Agilent VNMRS NMR instrument (750 MHz or 17.6 Tesla).

Neutron scattering

Small-angle neutron scattering (SANS) measurements were completed at room temperature using the Quokka small angle scattering instrument in the Australian Center for Neutron Scattering at ANSTO (the Australian Nuclear Science and Technology Organization). All Samples were prepared at ANSTO and sealed in quartz banjo cells with 1 mm path length. The isotropic two-dimensional (2D) scattering data were converted into one-dimensional scattering intensity as a function of the wavevector, $q = 4\pi\sin(\theta/2)/\lambda$, where λ is the neutron wavelength (λ = 6 Å) and θ is the scattering angle. The acquired scattering data were corrected for empty cell scattering, detector nonlinearity, electronic noise, stray scattering, sample transmission, and incoherent background scattering. Subsequently, the data were normalized to absolute differential scattering cross-section and reported in cm^{-1}.

Electrode preparation

UME and SECM substrates were fabricated following the procedure described in our previous work [8]. Here, we provide a brief description of the SECM substrate fabrication process. A rectangular piece of roughly 25 × 15 mm was cut from a microscope glass slide. The pieces were degreased by rinsing in the following order: acetone, isopropanol, DI water, and isopropanol, then dried with compressed nitrogen gas. After this, the glass piece was plasma cleaned for 5 min. For sputtering, a portion of roughly 10 × 15 mm of each slide was covered with tape. A 15 nm layer of chromium, followed by a 60 nm platinum layer, was then sputtered on top. After the coating process, the tape was removed to expose the glass surface. Before any connections were made, the sputtered samples were cleaned and degreased using the previously mentioned procedure, and then plasma cleaned following the same process. A small piece of indium wire was interposed between the copper tape and a small section of the sputtered platinum. After applying pressure, the connection was tested using a multimeter. Both the UME and the conductive side of the SECM substrate were cleaned electrochemically before the start of each experiment by cycling from

0 V to − 0.75 V (vs Ag/AgCl) for 99 cycles in 0.1 M KNO3 in phosphate buffer (pH 7) at 750 mVs^{-1}.

An aqueous solution of 1 mM FcMeOH and 0.1 M KNO_3 in pH 7 phosphate buffer was employed to characterize the performance of our SECM tip by comparing it with mass-transfer-limited positive and negative feedback approach curves, as shown in Fig. S1. The dual conformation of the fabricated substrates enabled characterization of the tip by first approaching the glass insulating surface, then the sputtered Pt surface. Fittings of these curves showed that RG = 3, and we were able to confidently approach the surface at L = 0.35, which is approximately a 500 nm distance between the tip and substrate; the approach curves leading to this fit are observed in Fig. S1 [55]. The SECM tip electrode was slowly approached using the stepper motors, employing an aqueous solution of 1 mM FcMeOH in 0.1 M KNO_3 in a pH 7 phosphate buffer solution. The last approach was performed using the piezo motors, which were then retracted to their original place. The cell was rinsed 10 times with water, then rinsed twice with isopropanol. Immediately after, the cell was dried with compressed Ar gas for a few minutes to ensure every crevice was as dry as possible. The cell was rinsed with μE once, then filled with the same μE for the measurements.

Signal analysis

We followed the methodology reported in a previous publication [8]. Briefly, four amperometric curves of 270 s were recorded. Using a Python script, the first 30 s of each curve corresponding to the transient were discarded, and the remaining 240 s were binned into four segments of 60 s. For each of the resulting 16 segments, the power spectral density (PSD) was computed by taking the Fourier transform (only the positive frequencies), multiplying by the complex conjugate, and dividing by the number of points (600 per segment). This resulted in 16 individual PSDs, which were averaged out to obtain the final result.

Potential-controlled bulk electrolysis

The μE was placed in the center compartment of a W-cell with a 2 mL capacity. At the same time, the side chambers were filled with an aqueous solution containing the same supporting electrolyte and concentration as the one employed in the μE. In one compartment, a carbon rod was placed as the counter electrode, and in the opposite compartment, the Ag/AgCl (3 M KCl) reference electrode was placed via a 0.1 M $NaClO_4$|agar salt bridge. Bulk electrolysis was performed by applying a potential 0.5 V more positive than the $E_{1/2}$ for 4 h to oxidize the dissolved Fc, while stirring with a Teflon-coated stirrer driven by a magnetic stirring plate. Once done, a potential 0.5 V more negative than the $E_{1/2}$ was applied for another 4 h to reduce all the Fc^+ generated. This oxidation and reduction process was repeated three times. The charge capacity (%) was calculated as:

$$\text{Charge}(\%) = \frac{Q_{\text{Exp}}}{Q_{\text{Theory}}} \times 100\%,$$

where Q_{Exp} is the charge obtained during the bulk electrolysis, and Q_{Theory} is the theoretical charge available from the one-electron oxidation and reduction of the ferrocene in solution.

Acknowledgments

This work was supported as part of the Breakthrough Electrolytes for Energy Storage and Systems (BEES2), an Energy Frontier Research Center funded by the U.S. Department of Energy, Office of Science, Basic Energy Sciences under Award # DE-SC0019409. This work was carried out in part in the Materials Research Laboratory Central Research Facilities, and the School of Chemical Sciences NMR Laboratory at the University of Illinois. We acknowledge the support of the Australian Centre for Neutron Scattering, ANSTO, and the Australian Government through the National Collaborative Research Infrastructure Strategy, in supporting the neutron research infrastructure used in this work via ACNS proposal 18852. We also thank Josh King at ANSTO for his help in setting up Quokka, running the experiments, and reducing the data in the SANS instruments.

Author contributions

Armando Santiago-Carboney: Conceptualization, Formal Analysis, Investigation, Methodology, Original Draft Preparation. Mrinalini K. Ayilliath Kolaprath: Investigation. Adam Imel: Formal Analysis, Review & Editing. Mark Dadmun: Formal Analysis, Review & Editing. Joaquín Rodríguez-López: Conceptualization, Funding Acquisition, Supervision, Review & Editing.

Funding

Breakthrough Electrolytes for Energy Storage and Systems (BEES2), an Energy Frontier Research Center funded by the U.S. Department of Energy, Office of Science, Basic Energy Sciences under Award # DE-SC0019409.

Data availability

The data is available online in the supplementary material as a .zip file.

Declarations

Conflict of Interest The authors report no conflicts of interest.

Supplementary material

The online version of this article (https://doi.org/10.1557/s43578-026-01807-8) contains supplementary material, which is available to authorized users.

Open Access

References

1. M. Shoaib, P. Vallayil, N. Jaiswal, P. Iyapazham Vaigunda Suba, S. Sankararaman, K. Ramanujam, V. Thangadurai, Advances in redox flow batteries – a comprehensive review on inorganic and organic electrolytes and engineering perspectives. Adv. Energy Mater. **14**, 2400721 (2024)
2. B. Liu, Y. Li, G. Jia, T. Zhao, Recent advances in redox flow batteries employing metal coordination complexes as redox-active species. Electrochem. Energ. Rev. **7**(1), 7 (2024)
3. H. Hu, M. Han, J. Liu, K. Zheng, Z. Zou, Y. Mu, F. Yu, W. Li, L. Wei, L. Zeng, T. Zhao, Strategies for improving the design of porous fiber felt electrodes for all-vanadium redox flow batteries from macro and micro perspectives. Energy Environ. Sci. **18**(7), 3085 (2025)
4. V. Muñoz-Perales, M. van der Heijden, V. de Haas, J. Olinga, M. Vera, A. Forner-Cuenca, Understanding the role of electrode thickness on redox flow cell performance. ChemElectroChem **11**(2), e202300380 (2024)
5. S. Ahn, A. Yun, D. Ko, V. Singh, J. Min Joo, H. Ryung Byon, Organic redox flow batteries in non-aqueous electrolyte solutions. Chem. Soc. Rev. **54**(2), 742 (2025)
6. W. Sharmoukh, Redox flow batteries as energy storage systems: materials, viability, and industrial applications. RSC Adv. **15**(13), 10106 (2025)
7. A.E. Imel, B. Barth, D.G. Hayes, M. Dadmun, T. Zawodzinski, Microemulsions as emerging electrolytes: the correlation of structure to electrochemical response. ACS Appl. Mater. Interfaces **14**(17), 20179 (2022)
8. A. Santiago-Carboney, F. Konstantinov, M.A. Pence, B. Barth, A. Imel, T. Zawodzinski, J. Rodríguez-López, Correlation between microscopic current fluctuations observed at ultra-microelectrodes and macroscopic bulk electrolysis performance in redox-active microemulsions. J. Electrochem. Soc. **171**(11), 110502 (2024)
9. J. Klier, C.J. Tucker, T.H. Kalantar, D.P. Green, Properties and applications of microemulsions. Adv. Mater. **12**(23), 1751 (2000)
10. B.A. Barth, A. Imel, K.M. Nelms, G.A. Goenaga, T. Zawodzinski, Microemulsions: breakthrough electrolytes for redox flow batteries. Front. Chem. **10**, 831200 (2022)
11. J. Peng, N.M. Cantillo, Y. Xiao, K.M. Nelms, L.S. Roberts, G. Goenaga, A. Imel, B.A. Barth, M. Dadmun, D.G. Hayes, T. Zawodzinski, Decoupling conductivity and solubility in electrolytes using microemulsions. J. Electrochem. Soc. **168**(8), 080502 (2021)
12. M. Hejazifar, O. Lanaridi, K. Bica-Schröder, Ionic liquid based microemulsions: a review. J. Mol. Liq. **303**, 112264 (2020)
13. J. Xu, L. Zhang, A. Yin, W. Hou, Y. Yang, Nonaqueous ionic liquid microemulsions of 1-butyl-3-methylimidazolium tetrafluoroborate, toluene and ethanol. Soft Matter **9**(28), 6497 (2013)
14. N. Li, Y. Gao, L. Zheng, J. Zhang, L. Yu, X. Li, Studies on the micropolarities of bmimBF4/TX-100/Toluene ionic liquid microemulsions and their behaviors characterized by UV–Visible spectroscopy. Langmuir **23**(3), 1091 (2007)
15. F.E. Berger Bioucas, T.M. Koller, A.P. Fröba, Effective thermal conductivity, effective viscosity, and particle diffusion coefficient of microemulsions consisting of water, *n*-decane, and a non-ionic surfactant in different regions of the phase diagram. Int. J. Heat Mass Transf. **232**, 125901 (2024)
16. F.E.B. Bioucas, T.M. Koller, A.P. Fröba, Effective thermal conductivity of microemulsions consisting of water micelles in *n*-decane. Int. J. Heat Mass Transfer **200**, 123526 (2023)
17. X.-W. Li, J. Zhang, L.-Q. Zheng, B. Chen, L.-Z. Wu, F.-F. Lv, B. Dong, C.-H. Tung, Microemulsions of N-alkylimidazolium ionic liquid and their performance as microreactors for the photocycloaddition of 9-substituted anthracenes. Langmuir **25**(10), 5484 (2009)
18. D. Jiang, L. Chen, A. Wang, Z. Yan, Esterification of oleic acid in [Bmim]BF4/[Hmim]HSO4 + TX-100/cyclohexane ionic liquid microemulsion. RSC Adv. **4**(97), 54427 (2014)
19. G.-P. Zhou, Y. Zhang, X.-R. Huang, C.-H. Shi, W.-F. Liu, Y.-Z. Li, Y.-B. Qu, P.-J. Gao, Catalytic activities of fungal oxidases in hydrophobic ionic liquid 1-butyl-3-methylimidazolium hexafluorophosphate-based microemulsion. Colloids Surf. B Biointerfaces **66**(1), 146 (2008)
20. Y. Li, Q. Qiang, X. Zheng, Z. Wang, Controllable electrochemical synthesis of Ag nanoparticles in ionic liquid microemulsions. Electrochem. Commun. **58**, 41 (2015)

21. H. Zhang, Z. Hu, M. Li, L. Hu, S. Jiao, A high-performance supercapacitor based on a polythiophene/multiwalled carbon nanotube composite by electropolymerization in an ionic liquid microemulsion. J. Mater. Chem. A **2**(40), 17024 (2014)
22. C. Wang, J. Zhu, D. Zhang, Y. Yang, L. Zheng, Y. Qu, X. Yang, X. Cui, Ionic liquid – microemulsions assisting in the transdermal delivery of Dencichine: preparation, *in-vitro* and *in-vivo* evaluations, and investigation of the permeation mechanism. Int. J. Pharm. **535**(1), 120 (2018)
23. Q.-X. Mao, H. Wang, Y. Shu, X.-W. Chen, J.-H. Wang, A dual-ionic liquid microemulsion system for the selective isolation of hemoglobin. RSC Adv. **4**(16), 8177 (2014)
24. W. Qi, Y. He, M. Li, W. Chen, J. Yang, L. Zhao, Fabrication strategy of MXenes through ionic-liquid-based microemulsions toward supercapacitor electrodes. Langmuir **38**(45), 13995 (2022)
25. Q. Fan, R. Zhao, M. Yi, P. Qi, C. Chai, H. Ying, J. Hao, Ti3C2-MXene composite films functionalized with polypyrrole and ionic liquid-based microemulsion particles for supercapacitor applications. Chem. Eng. J. **428**, 131107 (2022)
26. K. Matuszek, S.L. Piper, A. Brzęczek-Szafran, B. Roy, S. Saher, J.M. Pringle, D.R. MacFarlane, Unexpected energy applications of ionic liquids. Adv. Mater. **36**(23), 2313023 (2024)
27. Z. Lei, C. Dai, J. Hallett, M. Shiflett, Introduction: ionic liquids for diverse applications. Chem. Rev. **124**(12), 7533 (2024)
28. K. Xue, X. Zhang, X. Sun, K. Su, Y. Wang, J. Lang, Z. Zheng, Di-imidazolium ionic liquid based electrolytes for high voltage electrochemical double layer capacitors. J. Energy Storage **83**, 110473 (2024)
29. H. Kaur, A. Thakur, R.C. Thakur, A. Kumar, A review on multi-faceted role of ionic liquids in modern energy storage systems: from electrochemical performance to environmental sustainability. Energy Fuels **39**(8), 3703 (2025)
30. M.V. Fedorov, A.A. Kornyshev, Ionic liquids at electrified interfaces. Chem. Rev. **114**(5), 2978 (2014)
31. O.K. Coskun, M. Muñoz, S. Dongare, W. Dean, B.E. Gurkan, Understanding the electrode–electrolyte interfaces of ionic liquids and deep eutectic solvents. Langmuir **40**(7), 3283 (2024)
32. A. Asserghine, S. Kim, T.P. Vaid, A. Santiago-Carboney, A.J. McNeil, J. Rodríguez-López, Ionic strength impacts charge capacity in a redox-matched flow battery: from single-particle interrogation to battery cycling. ACS Energy Lett. **9**(6), 2826 (2024)
33. D.O. Kim, A. Mishra, M. Zorigt, Y. Li, R.T. Haasch, J. Rodríguez-López, Potential dependent degradation of spinel LiMn2O4 (LMO) and related structures assessed via manganese- and oxygen-sensitive scanning electrochemical microscopy. J. Mater. Chem. A **13**(15), 10540 (2025)
34. S.T. Putnam, A. Santiago-Carboney, P. Qian, J. Rodríguez-López, Scanning electrochemical microscopy: an evolving toolbox for revealing the chemistry within electrochemical processes. Anal. Chem. **97**(15), 8147 (2025)
35. P.A. Winsor, Hydrotropy, solubilisation and related emulsification processes. Trans. Faraday Soc. **44**(0), 376 (1948)
36. J. Oberdisse, Introduction to soft matter and neutron scattering. EPJ Web Conf. **188**, 01001 (2018)
37. L. Arleth, J.S. Pedersen, Droplet polydispersity and shape fluctuations in AOT [bis(2-ethylhexyl)sulfosuccinate sodium salt] microemulsions studied by contrast variation small-angle neutron scattering. Phys. Rev. E (2001). https://doi.org/10.1103/PhysRevE.63.061406
38. G. Kaur, L. Chiappisi, S. Prévost, R. Schweins, M. Gradzielski, S.K. Mehta, Probing the microstructure of nonionic microemulsions with ethyl oleate by viscosity, ROESY, DLS, SANS, and cyclic voltammetry. Langmuir **28**(29), 10640 (2012)
39. M. Teubner, R. Strey, Origin of the scattering peak in microemulsions. J. Chem. Phys. **87**(5), 3195 (1987)
40. O. Regev, S. Ezrahi, A. Aserin, N. Garti, E. Wachtel, E.W. Kaler, A. Khan, Y. Talmon, A study of the microstructure of a four-component nonionic microemulsion by Cryo-TEM, NMR, SAXS, and SANS. Langmuir **12**(3), 668 (1996)
41. S. Xie, D.J. Meyer, E. Wang, F.S. Bates, T.P. Lodge, Structure and properties of bicontinuous microemulsions from salt-doped ternary polymer blends. Macromolecules **52**(24), 9693 (2019)
42. T. Sottmann, R. Strey, S.-H. Chen, A small-angle neutron scattering study of nonionic surfactant molecules at the water–oil interface: area per molecule, microemulsion domain size, and rigidity. J. Chem. Phys. **106**(15), 6483 (1997)
43. D. Herrera, T. Chevalier, D. Frot, L. Barré, A. Drelich, I. Pezron, C. Dalmazzone, Monitoring the formation kinetics of a bicontinuous microemulsion. J. Colloid Interface Sci. **609**, 200 (2022)
44. S.-Y. Tseng, R. Strey, U. Olsson, T. Sottmann, From regular solutions to microemulsions. Soft Matter **21**(19), 3839 (2025)
45. M. Monkenbusch, O. Holderer, H. Frielinghaus, D. Byelov, J. Allgaier, D. Richter, Bending moduli of microemulsions; comparison of results from small angle neutron scattering and neutron spin-echo spectroscopy. J. Phys. Condens. Matter **17**(31), S2903 (2005)
46. O. Holderer, H. Frielinghaus, M. Monkenbusch, M. Klostermann, T. Sottmann, D. Richter, Experimental determination of bending rigidity and saddle splay modulus in bicontinuous microemulsions. Soft Matter **9**(7), 2308 (2013)
47. T. Kenjo, R.M. Diamond, Hydration of perchlorate, tetraphenylboride, and nitrate ions in some organic solvents. J. Phys. Chem. **76**(17), 2454 (1972)
48. T. Kenjo, R.M. Diamond, Hydration of the halide ions in certain organic solvents. J. Inorg. Nucl. Chem. **36**(1), 183 (1974)
49. P.A. Bergstroem, J. Lindgren, O. Kristiansson, An IR study of the hydration of perchlorate, nitrate, iodide, bromide, chloride and

sulfate anions in aqueous solution. J. Phys. Chem. **95**(22), 8575 (1991)
50. L.M. Prince, *Microemulsions Theory and Practice* (Academic Press, New York, 1977)
51. A. Deyko, S.G. Hessey, P. Licence, E.A. Chernikova, V.G. Krasovskiy, L.M. Kustov, R.G. Jones, The enthalpies of vaporisation of ionic liquids: new measurements and predictions. Phys. Chem. Chem. Phys. **14**(9), 3181 (2012)
52. J. Dwan, D. Durant, K. Ghandi, Nuclear magnetic resonance spectroscopic studies of the trihexyl (tetradecyl) phosphonium chloride ionic liquid mixtures with water. Open Chem. **6**(3), 347 (2008)
53. E.V. Brovč, S. Pajk, R. Šink, J. Mravljak, Comparison of the NMR and the acid value determination methods for quality control of input polysorbates. Acta Chim. Slov. **66**(4), 934 (2019)
54. J. Peng, N.M. Cantillo, K.M. Nelms, L.S. Roberts, G. Goenaga, A. Imel, B.A. Barth, M. Dadmun, L. Heroux, D.G. Hayes, T. Zawodzinski, Electron transfer in microemulsion-based electrolytes. ACS Appl. Mater. Interfaces **12**(36), 40213 (2020)
55. C. Lefrou, R. Cornut, Analytical expressions for quantitative scanning electrochemical microscopy (SECM). ChemPhysChem **11**(3), 547 (2010)
56. N. Nioradze, J. Kim, S. Amemiya, Quasi-steady-state voltammetry of rapid electron transfer reactions at the macroscopic substrate of the scanning electrochemical microscope. Anal. Chem. **83**(3), 828 (2011)
57. P.S. Singh, H.-S.M. Chan, S. Kang, S.G. Lemay, Stochastic amperometric fluctuations as a probe for dynamic adsorption in nanofluidic electrochemical systems. J. Am. Chem. Soc. **133**(45), 18289 (2011)
58. A. Yochelis, M.B. Singh, I. Visoly-Fisher, Coupling bulk and near-electrode interfacial nanostructuring in ionic liquids. Chem. Mater. **27**(12), 4169 (2015)
59. K. Karu, E.R. Nerut, X. Tao, S.A. Kislenko, K. Pohako-Esko, I.V. Voroshylova, V.B. Ivaništšev, Ionic liquid–electrode interface: classification of ions, saturation of layers, and structure-determined potentials. Electrochim. Acta **503**, 144829 (2024)